CrossMark

The Resolved Star Formation Law in NGC 7469 from JWST, ALMA, and VLA

Maria Vittoria Zanchettin[1,2] , Marcella Massardi[3] , Francesco Salvestrini[2] , Manuela Bischetti[2,4] , Chiara Feruglio[2,5] ,
Fabrizio Fiore[2,5] , and Andrea Lapi[1,3,5,6]

[1] SISSA, Via Bonomea 265, I-34136 Trieste, Italy; mazanch@sissa.it
[2] INAF Osservatorio Astronomico di Trieste, via G.B. Tiepolo 11, 34143 Trieste, Italy
[3] INAF, Istituto di Radioastronomia, Italian ARC, Via Piero Gobetti 101, I-40129 Bologna, Italy
[4] Dipartimento di Fisica, Università di Trieste, Sezione di Astronomia, Via G.B. Tiepolo 11, I-34131 Trieste, Italy
[5] IFPU—Institute for Fundamental Physics of the Universe, Via Beirut 2, 34014 Trieste, Italy
[6] INFN, Sezione di Trieste, via Valerio 2, Trieste I-34127, Italy

Abstract

We investigate the star formation process within the central 3.3 kpc region of the nearby luminous infrared Seyfert NGC 7469, probing scales ranging from 88 to 330 pc. We combine JWST/MIRI imaging with the F770W filter, with $CO(2-1)$ and the underlying 1.3 mm dust continuum data from the Atacama Large Millimeter/submillimeter Array, along with Karl G. Jansky Very Large Array radio continuum observations at 22 GHz. NGC 7469 hosts a starburst ring which dominates the overall star formation activity. We estimate the global star formation rate (SFR) $\sim 11.5\ M_\odot\ \mathrm{yr}^{-1}$ from the radio at 22 GHz, and a cold molecular gas mass $M(\mathrm{H}_2) \sim 6.4 \times 10^9\ M_\odot$ from the $CO(2-1)$ emission. We find that the 1.3 mm map shows a morphology remarkably similar to those traced by the 22 GHz and the 7.7 μm polycyclic aromatic hydrocarbon (PAH) emission observed with JWST. The three tracers reproduce the morphology of the starburst ring with good agreement. We further investigate the correlations between the PAHs, the SFR, and the cold molecular gas. We find a stronger correlation of the PAHs with star formation than with CO, with steeper correlations within the starburst ring ($n > 2$) than in the outer region ($n < 1$). We derive a correlation between the SFR and the cold molecular gas mass surface densities, the Kennicutt–Schmidt (K-S) star formation law. Comparisons with other galaxy populations, including starburst galaxies and active galactic nuclei, highlighted that NGC 7469 exhibits an intermediate behavior to the K-S relations found for these galaxy populations.

1. Introduction

Schmidt (1959, 1963) proposed the existence of empirical scaling relations between the properties of the interstellar gas and the star formation rate (SFR) in the same environment. Later, Kennicutt (1998a, 1998b) confirmed the correlation between global measurements of galaxy gas mass and SFR in nearby galaxies. Consequently, this correlation has become known as the Kennicutt–Schmidt (K-S) star formation (SF) law.

Spatially unresolved studies that target molecular gas and SFR help to derive global disk properties and are necessary to test the redshift dependence of the gas–SF relation (Genzel et al. 2010; Schruba et al. 2011). However, to understand the physical mechanisms behind the SF process, spatially resolved measurements in nearby targets are necessary. These observations allow us to study how the SF properties, such as the timescales for gas consumption and the SF efficiency, vary across galaxy environments (Onodera et al. 2010; Bigiel et al. 2011; Ford et al. 2013; Leroy et al. 2013; Kreckel et al. 2018; Dey et al. 2019; Pessa et al. 2022; Sun et al. 2023). The tracers most commonly used to quantify the SFR are the most commonly observed optical spectral lines (e.g., Hα and [O II]), the global radio continuum, mid- and far-infrared (MIR and

FIR), and ultraviolet (UV) emission. Such SFR indicators refer to various wavelengths that trace stellar populations at different evolutionary stages (see Kennicutt & Evans 2012, for a review). Optical lines and UV light are emitted predominantly by young stars and are sensitive to SF on $\sim$10 Myr and $\sim$10–100 Myr timescales, respectively (Hao et al. 2011; Murphy et al. 2011). However, accurate SFR estimates from UV data are affected by large uncertainties due to the dust extinction correction (Mahajan et al. 2019). The thermal free–free and nonthermal synchrotron radio emission at low frequency (1–10 GHz) are a measure of the past formation of massive stars, resulting in an SF time sensitivity of about 150–300 Myr (Klein & Emerson 1981; Gioia et al. 1982; Tabatabaei et al. 2017; Arango-Toro et al. 2023). The MIR (3–25 μm) emission of star-forming galaxies is dominated by polycyclic aromatic hydrocarbon (PAH) features both at low and high redshift (Puget & Leger 1989; Genzel et al. 1998; Armus et al. 2007; Valiante et al. 2007; Farrah et al. 2008; Veilleux et al. 2009; Riechers et al. 2014). In particular, PAHs have been proposed as a good indicator of SFR over timescales of up to a few hundred million years (Peeters et al. 2004; Shipley et al. 2016; Xie & Ho 2019). Moreover, a connection between PAHs and the properties of the cold molecular gas, as traced by CO emission, has been proposed by several studies (Cortzen et al. 2019; Alonso-Herrero et al. 2020). Taking advantage of interferometric millimeter and centimeter, and James Webb Space Telescope (JWST), data of nearby galaxies, it is possible to perform spatially resolved studies of the SF process in galaxies, down to 100 pc scales and to investigate
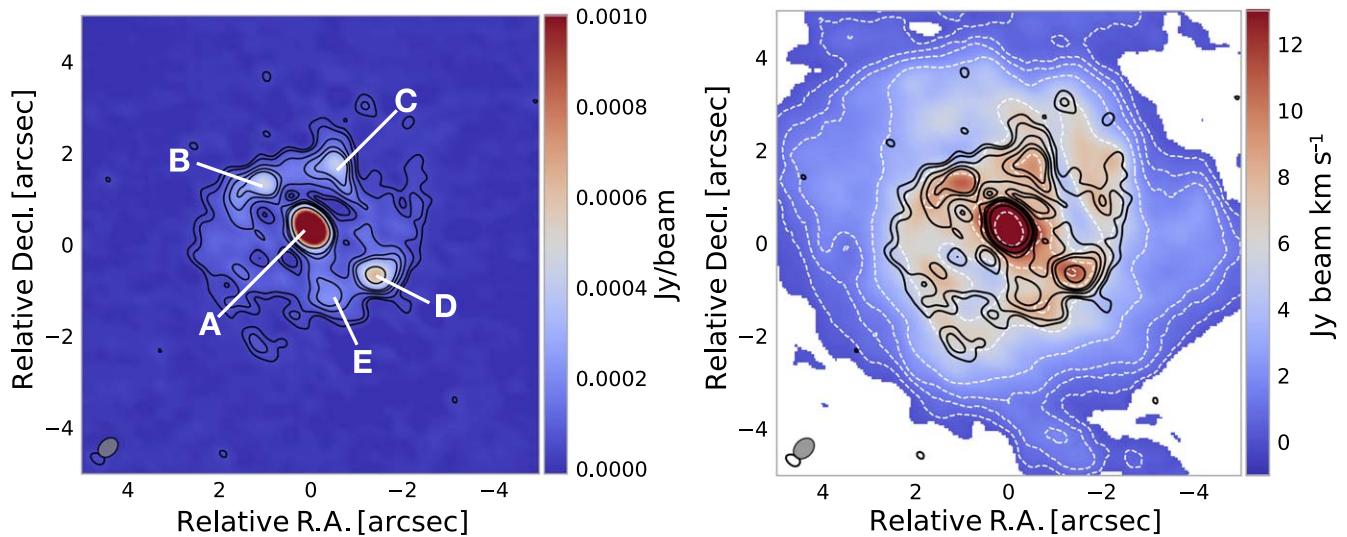
Figure 1. Left panel: 1.3 mm continuum map. Labels from A to E indicate the five clumps of emission. The position of A corresponds to the AGN position (23:03:15.617, +08:52:26.00 (J2000); Izumi et al. 2020). Contours are drawn at $(3, 5, 10, 15, 20, 40)\sigma$, where $\sigma = 0.0121$ mJy beam^{-1}. The clean beam $(0\rlap{.}''492 \times 0\rlap{.}''360$, position angle (PA) = 46°) is indicated by the gray ellipse. Right panel: velocity-integrated CO(2 − 1) (moment 0) map. White contours are drawn at $(3, 5, 10, 15, 20, 30)\sigma$, where $\sigma = 0.56$ Jy beam^{-1} km s^{-1}. The clean beam $(0\rlap{.}''508 \times 0\rlap{.}''374$, PA = 45°) is indicated by the gray ellipse. Regions with emission below 1σ are blanked out.

the correlations between PAHs, the SFR surface density ($\Sigma_{\rm SFR}$), and the mass surface density of molecular gas ($\Sigma_{\rm H2}$), which is the direct fuel for the formation of stars.

In this paper, we study the SF process in the inner ($\sim$3 kpc) region of NGC 7469, a nearby ($z = 0.01627$) luminous infrared galaxy (LIRG; $L_{\rm IR,8-1000~\mu m} = 10^{11.6}~L_\odot$), and type-1.5 Seyfert (Landt et al. 2008) with a bolometric active galactic nucleus (AGN) luminosity of $L_{\rm bol,AGN} = 3.5 \times 10^{44}$ erg s^{-1} (Gruppioni et al. 2016). From Karl G. Jansky Very Large Array (VLA) 8.4 GHz observations at $0\rlap{.}''3$ resolution, Pérez-Torres et al. (2009) estimated the nuclear radio emission $L_{\rm 8.4~GHz} \sim 10^{36.96}$ erg s^{-1}. NGC 7469 may host a radio core jet structure as resolved on a $0\rlap{.}''3$ scale by the VLA (Lonsdale et al. 2003; Alberdi et al. 2006; Orienti & Prieto 2010), and no evidence of a radio jet–interstellar medium (ISM) interaction has yet been reported (Xu & Wang 2022). NGC 7469 is known to host a prominent starburst (SB) ring with an outer radius of 900 pc, which dominates the global SFR of $\sim$20−50 $M_\odot$ yr^{-1} (Genzel et al. 1995; Soifer et al. 2003; Gruppioni et al. 2016; Song et al. 2021). A bar-like feature connects the SB ring to a circum-nuclear disk (CND) located in the inner 300 pc (see Davies et al. 2004; Izumi et al. 2015, 2020, and references therein). The molecular gas mass derived from CO(1 − 0) within the inner $\sim$1.2 kpc region is $M({\rm H_2}) = 2.7 \times 10^9~M_\odot$ (Davies et al. 2004; Izumi et al. 2020). To investigate the SF process inside and outside the SB ring of NGC 7469, we combine JWST imaging with the F770W filter of the Mid-InfraRed Instrument (MIRI), with CO(2 − 1) and the underlying dust continuum (224.2–243.7 GHz) data obtained from the Atacama Large Millimeter/submillimeter Array (ALMA), along with the VLA radio continuum imaging at 22 GHz, resolving physical scales in the range 88 pc (MIRI) to 330 pc (VLA).

This paper is organized as follows. In Section 2, we describe the observations and data reduction. Section 3 provides details on the data analysis and quantity derivations. Section 4 describes our results. The adopted luminosity distance of the galaxy is 72.1 Mpc and the corresponding scale is 0.338 kpc arcsec^{-1}.

2. Observations and Data Reduction

We analyzed band 6 ALMA 12 m observations (program ID 2017.1.00078.S, PI: Izumi Takuma) of NGC 7469 of the CO(2 − 1) line (observed frequency of 226.85 GHz) and the underlying continuum (224.2–243.7 GHz). NGC 7469 was observed in 2018 September by using the 12 m array for a total integration time of 1.48 hr in the configuration C43-4 with 44 antennas, proving an angular resolution of about $0\rlap{.}''4$ and a largest angular scale of $4\rlap{.}''8$. Visibilities were calibrated by the NRAO, using the standard pipeline and default calibrators. Imaging was performed with the Common Astronomy Software Applications (CASA; McMullin et al. 2007), version 5.1.1–5. We created a continuum map by averaging the visibilities in the four spectral windows (spws), excluding the spectral range covered by the CO(2 − 1) emission line. We produced continuum-subtracted data cubes by fitting and subtracting a first-order polynomial from the visibilities of the spw covering CO(2 − 1). Imaging was performed with the task `tclean` using the `hogbom` algorithm, a threshold of 3 times the rms noise, a Briggs weighting scheme with robust parameter $b = 0.5$ for the continuum map, and a natural weighting scheme for the CO(2 − 1) data cube in order to increase the map sensitivity. The resulting synthesized beam for the continuum map is $0\rlap{.}''492 \times 0\rlap{.}''360$ (corresponding to 164 pc × 120 pc), with an rms of 0.0121 mJy beam^{-1}. The CO(2 − 1) data cube has a beam size of $0\rlap{.}''508 \times 0\rlap{.}''374$ and a rms noise of 0.518 mJy beam^{-1} for a channel width of 5 km s^{-1}. This translates into a mass surface density sensitivity of 7.8 $M_\odot$ beam^{-1} for a channel width of 5 km s^{-1}, computed using Equation (1). Figure 1 shows (left panel) the millimeter continuum map and (right panel) the continuum-subtracted velocity-integrated map of the CO(2 − 1) emission.

We analyzed archival VLA observations of NGC 7469 in the K band (project code 20A-158, PI: Krista L. Smith). The observations were carried out in 2020 April for a total integration time of 58.9 hr in the frequency range 18–26 GHz. We used the standard calibrated visibilities provided by the VLA data archive l[7] and we used CASA 5.1.1-5 software to generate the map of

---

7 https://science.nrao.edu/facilities/vla/archive
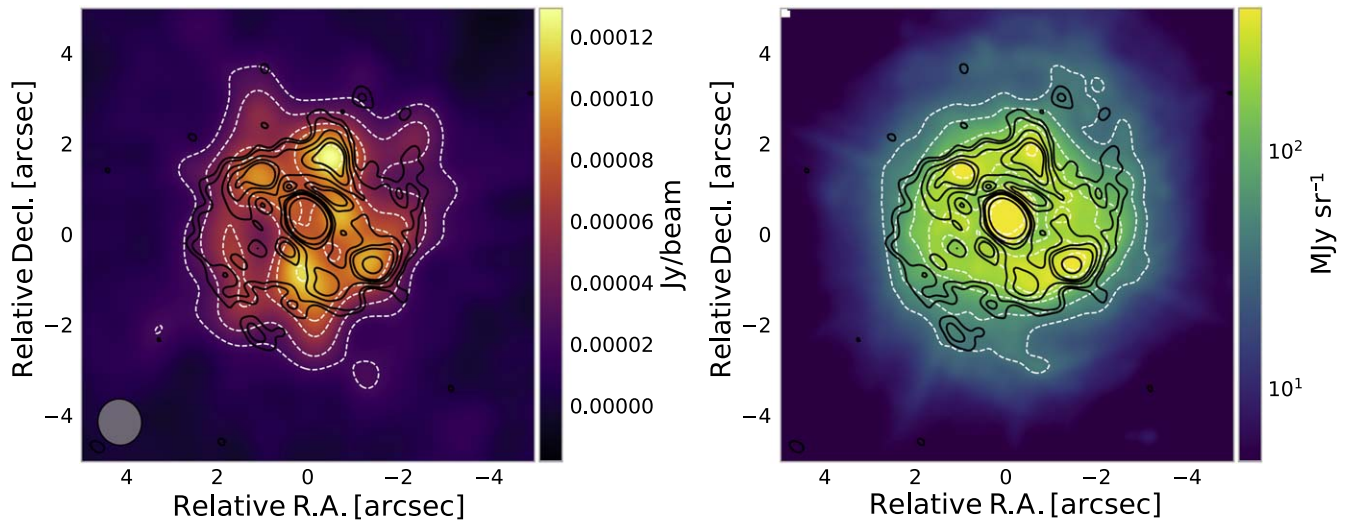
Figure 2. Left panel: VLA 22 GHz radio continuum map (color scale), with corresponding white contours drawn at $(3, 5, 8, 10, 15)\sigma$, where $\sigma = 0.023$ mJy beam^{-1}. The clean beam ($1\rlap{.}''03 \times 0\rlap{.}''97$, PA $= -13°$) is indicated by the gray ellipse. Right panel: JWST MIRI/F770W image (color scale), with white contours drawn at $(3, 5, 10, 15, 20, 30, 50)\sigma$, where $\sigma = 27$ MJy sr^{-1}. The black contours in both panels show the 1.3 mm continuum emission (same as in Figure 1, left panel).

the K-band continuum. We averaged the 62 spws and we produced a clean map using the `tclean` task and a Briggs weighting scheme with robust parameter $b = 0.5$. We used the `hogbom` cleaning algorithm with a detection threshold of 3 times the rms sensitivity. The final continuum map has an rms of 23.2 μJy beam^{-1} and a clean beam of $1\rlap{.}''029 \times 0\rlap{.}''967$ (i.e., 342 pc × 322 pc).

JWST/MIRI (Bouchet et al. 2015; Rieke et al. 2015) imaging of NGC 7469 was obtained with the F770W (7.7 μm) filter with both the BRIGHTSKY and SUB128 subarray modes (program ID 1328, PI: Armus Lee). In this paper we focus the analysis on the SUB128 subarray data, where the nucleus remained unsaturated, taken on 2022 July 2 with an exposure time of 48 s. The field of view is $14\rlap{.}''8 \times 16\rlap{.}''4$ and the pixel size is $0\rlap{.}''11$. The calibrated JWST/MIRI 7.7 μm map has a sensitivity of 12 MJy sr^{-1} pixel^{-1}. We used the calibrated images provided by the STScI, downloaded through the MAST portal.[8]

3. Analysis

Within CASA, we modeled and subtracted the central point-source emission in the VLA map to remove its contribution from the circumnuclear region. We used the task `os.system` to model a point source at the AGN position (23:03:15.617, +08:52:26.00 (J2000); Izumi et al. 2020) with a flux of 5.037 mJy at 22 GHz, corresponding to 90% of the central beam flux. We performed several tests with different point-source flux normalizations, and checked that with the assumed fraction we avoid artificial oversubtracted regions. The final circumnuclear region flux is corrected by 15% and its value is consistent with the central beam flux after point-source subtraction. We used the `uvsub` task to subtract the point-source model from the visibility data, so obtaining the final visibilities. We followed the cleaning procedure described in Section 2 to obtain the final map reported in Figure 2, left panel.

We used the WebbPSF[9] tool version 1.2.1 (Perrin et al. 2014) to simulate the point-spread function (PSF) of the

JWST/MIRI F770W filter image, with a pixel size of $0\rlap{.}''027$. We modeled the radial PSF contribution by using circular sectors with a radius equal to the grid cell size, see Section 3, and we derived the radial correction for the F770W filter map. We corrected both the F770W filter fluxes extracted with the grid and their associated errors for the PSF contribution according to their distance from the center, by following standard error propagation (i.e., convolving the square of the error map with the square of the PSF error). Due to the limitations in the current theoretical model for the JWST PSF, we do not have a robust method for removing the PSF spikes (see Williams et al. 2024, and references therein). Therefore we applied this conservative method to subtract and model the PSF contribution. We excluded from the analysis the central $1''$ (~330 pc) region where the PSF contribution is dominant.

We used the continuum-subtracted velocity-integrated CO(2 – 1) line intensity map to derive the mass surface density of the cold molecular gas, the VLA radio map at 22 GHz to estimate the SFR surface density, and the JWST/MIRI F770W filter map to estimate the PAH emission at 7.7 μm. Since we analyzed one single PAH feature at 7.7 μm, we omit the 7.7 μm wording from this point onward. We extract fluxes from a common grid applied to all maps. First, we regridded all the maps at the VLA spatial resolution, i.e., the coarsest resolution of all our data. The grid is centered at the AGN position and has $1''$ wide (i.e., 0.330 kpc) square cells, equal to the regridded map resolution, and a total size of $10'' \times 10''$ (i.e., 3.3 kpc × 3.3 kpc). Fluxes are extracted from each cell. If the mean flux in the cell is below $3 \times$ rms per pixel, we consider it as an upper limit. For each grid cell, we derived the corresponding cold molecular gas mass (M_{H2}) surface density (Σ_{H2}), SFR surface density (Σ_{SFR}), and PAH flux density (Σ_{PAH}). The central cell (i.e., the one that contains the AGN) is not used, since it is not possible to determine and disentangle the AGN contribution to the measured flux with good accuracy. Indeed, in this region, we expect both a significant contribution in the JWST image arising from dust-reprocessed AGN emission from the torus, and a possible contribution to the VLA continuum due to the presence of a core jet-like structure (Lonsdale et al. 2003; Alberdi et al. 2006). We note that Armus et al. (2023) verified that in the total MIR spectrum of

---

[8] https://mast.stsci.edu/portal/Mashup/Clients/Mast/Portal.html
[9] https://webbpsf.readthedocs.io

NGC 7469 PAH emissions are significantly weaker at the nucleus, due to the AGN heating effect. They reported that the SFR from PAH in the nuclear region, i.e., a $0\rlap{.}''3$ (~100 pc) diameter circular region, is less than 1% of the total SFR in NGC 7469.

The Σ_{H2} in units of $M_\odot$ pc^{-2} is derived from the velocity-integrated CO(2 – 1) flux density as

$$\Sigma_{H2} = \alpha_{CO} \frac{S_{CO(2-1)}}{R_{21}} F_{21} \cos i, \qquad (1)$$

where F_{21} is a conversion factor from the flux density to the line luminosity L' in units of K km s^{-1} pc^2 (see Solomon & Vanden Bout 2005), i is the galaxy inclination angle, and α_{CO} is the CO-to-H$_2$ conversion factor. We adopt a CO ladder correction factor of $R_{21} = 0.7$, equal to the mean value found by Casasola et al. (2015), and $\alpha_{CO} = 4.2^{+1.961}_{-1.341} M_\odot$(K km s^{-1} pc^2)$^{-1}$ derived adopting Equation (25) in Accurso et al. (2017), for a stellar mass of $\log(M_*/M_\odot) = 10.5$ (Díaz-Santos et al. 2007). The $\cos i$ factor is the correction for galaxy inclination, which we assume $i = 45°$ (Davies et al. 2004).

Assuming that most of the radio 22 GHz continuum emission arises from SF, we adopt the radio luminosity at 22 GHz to derive the SFR. First, we derived the radio luminosity at 1.4 GHz by assuming an average radio spectrum steepness of $\alpha = -0.85$ for the entire galaxy. We obtained the α parameter by fitting the radio spectral energy distribution using the integrated radio fluxes reported by the NASA/IPAC Extragalactic Database.[10] The α parameter adopted is consistent with the values used to describe SF regions in normal galaxies and LIRGs (e.g., Murphy et al. 2012; Linden et al. 2019, 2020) and with the values derived by Song et al. (2021). However, we cannot exclude local variations in the steepness of the radio spectrum that can affect the final SFR values. Song et al. (2021) derived the spectral index measured from 15 to 33 GHz, finding values in between ~-0.7 and ~-0.9 in the NGC 7469 nuclear ring. These variations translate into corrections to the SFR up to 10%, which will be taken into account further in the discussion. We then obtained the SFR adopting the correlation reported by Shao et al. (2018, Section 3.2), and the corresponding SF surface density, Σ_{SFR}, by correcting for galaxy inclination, i.e., multiplying by the $\cos i$ factor as in Equation (1).

The MIRI F770W allows us to sample the 7.7 μm PAH emission complex in NGC 7469. Although the band is dominated by the PAH emission feature, it may also include continuum emission due to hot dust. Whitcomb et al. (2023) showed that the Spitzer/IRS spectra of the star-forming regions in 75 nearby galaxies (SINGS sample) may have up to 10% continuum contamination in the F770W filter. Therefore, in a conservative approach, we assumed that 90% of the flux is attributed to PAHs (Chastenet et al. 2023).

4. Discussion and Conclusion

### 4.1. Morphology of the Starburst Ring

We estimate the global SFR integrated over the central 3.3 kpc × 3.3 kpc into SFR = 11.5 ± 0.3 $M_\odot$ yr^{-1}, following the prescription of Shao et al. (2018), see Section 3. This estimate does not include the contribution from the central 330 pc × 330 pc

---

10 https://ned.ipac.caltech.edu

cell. The uncertainty accounts for a realistic estimate of the systematic scatter in the 1.4 GHz-based method (~0.3 dex according to Shao et al. 2018). Our SFR estimate is consistent with the SFR = 21 ± 2.1 $M_\odot$ yr^{-1} values found by Song et al. (2021) from the 3–33 GHz radio continuum, and with the range of SFR = 10–30 $M_\odot$ yr^{-1} reported by Lai et al. (2022) using optical emission lines, namely the Pfα recombination line, [Ne II], and [Ne III]. We found that the majority, approximately 60%, of the SF occurs in the SB ring, consistent with Song et al. (2021).

We computed the molecular gas mass over the central 3.3 kpc × 3.3 kpc $M(H_2) = (6.4 \pm 2.0) \times 10^9$ $M_\odot$, where the error is dominated by the uncertainty on α_{CO} (0.165 dex; Accurso et al. 2017). This estimate is consistent within 2σ with the values reported in the literature using different CO transitions (Davies et al. 2004; Izumi et al. 2020; Nguyen et al. 2021; Zhang & Ho 2023). We note that these works focus on the inner ~1 kpc region of NGC 7469, i.e., the SB ring. We computed that $\sim50\%$ of the total cold molecular gas mass is contained in the SB ring, $M(H_2)_{SB} = (3.3 \pm 1.0) \times 10^9$ $M_\odot$. The central concentration of gas and SFR is in line with those observed in local LIRGs (Díaz-Santos et al. 2010, 2011). Adopting our estimate of $M(H_2)$ and SFR, we derived the characteristic gas depletion timescale, $\tau_{dep} = M(H_2)/$SFR. We obtained $\tau_{dep} = (0.56 \pm 0.18)$ Gyr for the central 3.3 kpc × 3.3 kpc region, and a shorter $\tau_{dep} = (0.47 \pm 0.15)$ Gyr for the SB ring. Considering the errors associated with the values, the depletion times are consistent within 1σ.

Figure 1 shows the distribution of the 1.3 mm continuum and the integrated CO(2 – 1) flux map (moment 0 map). In the continuum map, we identify five representative positions (A–E), that are detected as clumps with a signal-to-noise ratio (S/N) > 15. Clumps from A to D are named as in Izumi et al. (2020), who first identified the clumps using an ALMA 860 μm continuum map. In addition, we identify clump E (23:03:15.60, +08:52:24.56 (J2000)) where we detect 1.3 mm emission with a statistical significance of $\sim18\sigma$. The 1.3 mm central peak position, labeled as clump A, is consistent with the AGN position from VLA 3.5 cm and ALMA 860 μm continuum emission (Condon et al. 1991; Orienti & Prieto 2010; Izumi et al. 2020). Due to PSF smearing of the central AGN emission in MIRI 7.7 μm, we excluded from the following analysis the central cell, which contains also the CND (Davies et al. 2004; Izumi et al. 2015). Figure 2 shows the VLA 22 GHz emission map (left panel) and the JWST/MIRI PAH emission map (right panel), both with 1.3 mm emission contours overlaid. The 1.3 continuum map traces the dust distribution across the SB ring, which shows a morphology that is remarkably similar to those traced by PAHs and radio continuum at 22 GHz. The three tracers reproduce the morphology of the SB ring with good agreement. In particular, clumps B, C, and D are detected with similar morphology and size in the dust continuum, CO(2 – 1), 22 GHz, and the PAH emission. The overall clump distribution appears to be consistent also with the 860 μm continuum (Izumi et al. 2020), suggesting that the 1.3 mm emission is mainly tracing thermal dust emission heated by young stars in the SB ring. While the dusty clumps B, C, D, and E all show prominent counterparts also in the CO map (Figure 2), the dusty clump E exhibits no evident counterpart in the radio or MIR maps. Interestingly, the 22 GHz radio continuum map presents an emission peak with a significance of 15σ (23:03:15.63, +08:52:24.98 (J2000)), offset by about $0\rlap{.}''5$ with respect to E along the northeast direction (white and black contours in the left panel of Figure 3). We exclude a contribution
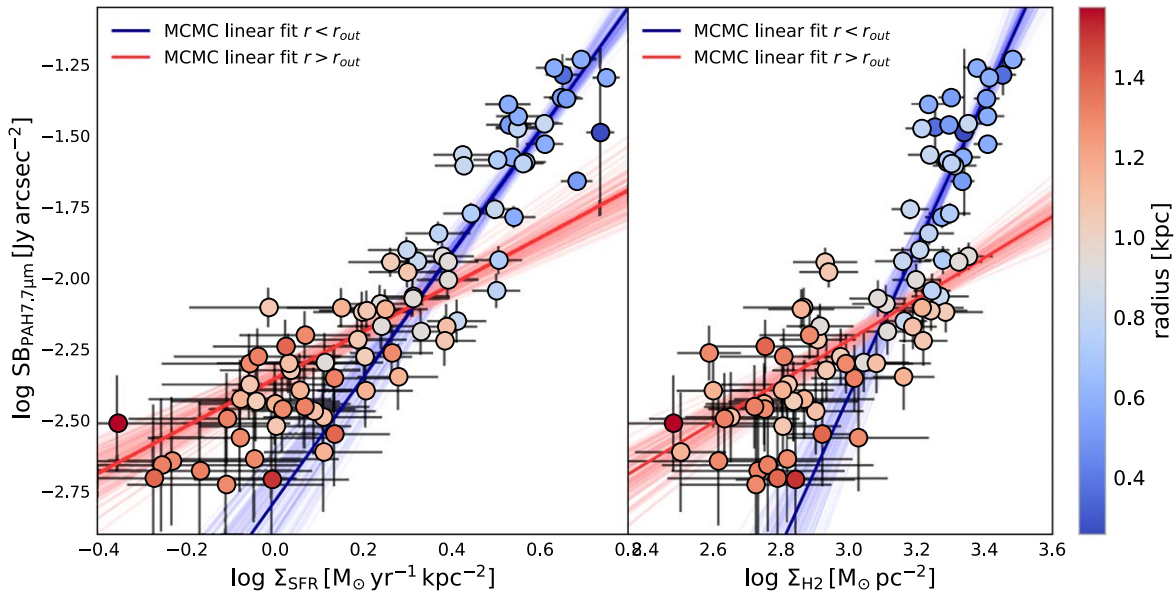
Figure 3. Surface brightness at 7.7 μm from JWST/MIRI imaging vs. Σ_{SFR} (left panel) and Σ_{H_2} (right panel), within the central $10'' \times 10''$ region of NGC 7469. The symbols are colored according to their distance from the galaxy center (color bar). The dashed blue (red) lines are the Markov Chain Monte Carlo (MCMC) linear fits to data for $r < r_{SB}$ ($r > r_{SB}$), where $r_{SB} \sim 900$ pc is the outer SB ring radius (Song et al. 2021).

Table 1
Derived Parameters for the Σ_{SFR}–SB$_{PAH}$ and Σ_{H2}–SB$_{PAH}$ Correlations

		Σ_{SFR}–SB$_{PAH}$				Σ_{H2}–SB$_{PAH}$			
Radius (a)	Number data points (b)	ρ (c)	τ (d)	n (e)	k (f)	ρ (c)	τ (d)	n (e)	k (f)
$r > 0$	82	0.91	0.75	1.77 ± 0.08	-2.56 ± 0.03	0.84	0.68	2.17 ± 0.11	-15.48 ± 0.36
$r < r_{SB}$	31	0.76	0.56	2.16 ± 0.20	-2.78 ± 0.02	0.71	0.52	2.61 ± 0.25	-10.25 ± 0.03
$r > r_{SB}$	51	0.77	0.56	0.83 ± 0.10	-2.36 ± 0.03	0.66	0.47	0.72 ± 0.09	-4.39 ± 0.03

Note. The columns report (a) the radius of the data points, (b) the number of data points, (c) the Pearson ρ correlation coefficient, (d) the Kendall τ rank correlation coefficient, (e) the slope n, and (f) the zero-point k of the linear fit $y = nx + k$.

from the unresolved radio jet at this location, as a core jet-like structure was only detected at the nucleus (Lonsdale et al. 2003; Alberdi et al. 2006). Indeed, the local enhancement in the radio emission may be attributed to a gas inflow associated to the SB ring and to the two-arm spiral structure, suggested by the high-velocity dispersion of the cold molecular gas at this location (Nguyen et al. 2021). Clumps B and D are located at the endpoints of a bar-like feature identified by Davies et al. (2004), Fathi et al. (2015), and Izumi et al. (2015). Although the bar structure is detected at a significance level of 12σ in the CO(2 − 1) map, it remains undetected down to 3σ in the radio continuum and in the 7.7 μm maps, despite the high angular resolution of JWST/MIRI.

4.2. Polycyclic Aromatic Hydrocarbon Emission

In the following, we investigate the correlation between Σ_{SFR}, Σ_{H_2}, and PAH surface brightness, SB$_{PAH}$. Figure 3 shows SB$_{PAH}$ versus Σ_{SFR} (left panel) and Σ_{H_2} (right panel), within the region of NGC 7469 sampled by the grid. The PAH surface brightness correlates both with the SFR and the cold molecular gas surface densities. We derived the Pearson ρ and the Kendall τ rank correlation coefficients (Table 1), finding a higher correlation of SB$_{PAH}$ with Σ_{SFR} than with Σ_{H_2}, both for the SB ring and for external regions. Although the S/N of the

radio map is lower than that of the CO map (Section 2), the correlation between SB$_{PAH}$ and Σ_{SFR} is stronger and narrower than that with Σ_{H2}. This is likely due to the PAH emission being more affected by the ionizing radiation field of young stars rather than by the availability of molecular gas (see Jensen et al. 2017; Belfiore et al. 2023, and references therein).

We also observe a steepening of both relations moving toward the center of the galaxy, as highlighted in Figure 3 by the color gradient of the symbols. To quantify this steepening, we divided the data into two subsamples: an inner region within the SB ring ($r < r_{SB}$) and an outer region with $r > r_{SB}$, where $r_{SB} = 900$ pc. This value has been measured by Song et al. (2021) using 3–30 GHz continuum and is consistent with our maps. We fit a linear relation $y = nx + k$ to each subsample using the Python package emcee (Foreman-Mackey et al. 2013), and assuming a constant error on Σ_{H2} and Σ_{SFR}, equal to the rms noise of each regridded map. The uncertainty associated to SB$_{PAH}$ is obtained by convolving the rms noise of the regridded MIRI map with the uncertainty due to the PSF contribution (Section 3). The blue and red solid lines in Figure 3 show the fits for $r < r_{SB}$ and for $r > r_{SB}$, respectively. For both Σ_{SFR} and Σ_{H2}, the SB ring shows a steeper slope with respect to $r > r_{SB}$ (Table 1). In particular, the slope at the SB ring is $n = (2.16 \pm 0.20)$ whereas at $r > r_{SB}$ is $n = (0.83 \pm 0.10)$. A similar behavior is seen for the Σ_{H2}
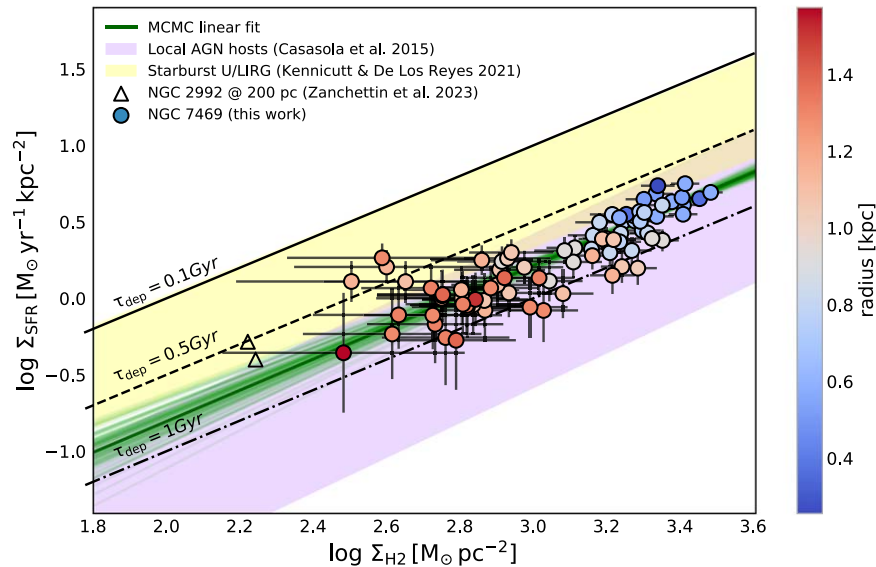
Figure 4. Spatially resolved SF law within the central $10'' \times 10''$ region of NGC 7469. Circles show the derived quantities in each cell of the grid, colored according to their distance from the AGN (color bar). The dashed green lines are the linear fit to the data $\log \Sigma_{SFR} = (1.02 \pm 0.07)\log \Sigma_{H2} + (-2.85 \pm 0.02)$, derived by using the Python `emcee` library (Foreman-Mackey et al. 2013). Triangles show the derived quantities for NGC 2992 (Zanchettin et al. 2023). The yellow shaded area shows the best-fit correlation with 0.33 dex scatter found using global measurements for (Kennicutt & De Los Reyes 2021): $\log \Sigma_{SFR} = (0.98 \pm 0.07)\log \Sigma_{H2} + (-2.27 \pm 0.21)$. The purple shaded area shows the range of values found by Casasola et al. (2015) for local AGN host galaxies: $\log \Sigma_{SFR} = (1.14 \pm 0.01)\log \Sigma_{H2} + (-3.41 \pm 0.02)$. Solid, dashed, and dotted black lines represent gas depletion times τ_{dep} of 0.1, 0.5, and 1 Gyr, respectively.

correlation. The steepening of these relations may be attributed to an enhancement of recent SF activity in the SB ring structure, as already observed using the 11.3 μm PAH feature by Jensen et al. (2017). This is consistent with the presence of a young population of ionizing stars in the SB ring, as reported by Díaz-Santos et al. (2007). Jensen et al. (2017) measured a negligible contribution of AGN-heated dust to the continuum flux at 11 μm above 200 pc. Therefore, we exclude that this steepening is due to an increased contribution of AGN-heated dust to the continuum emission measured in the JWST F770W filter, at the location of the SB ring. Regarding a possible AGN contribution to PAH destruction, we do not expect a significant effect given the modest luminosity of our target ($L_{bol,AGN} = 3.5 \times 10^{44}$ erg s^{-1}; Gruppioni et al. 2016).

Still, local variations in gas properties, including composition, turbulence, and metallicity, significantly influence the CO-to-H$_2$ conversion factor (Leroy et al. 2011; Narayanan et al. 2012; Papadopoulos et al. 2012; Bolatto et al. 2013; Sandstrom et al. 2013; Teng et al. 2024). Oxygen abundances compatible with solar metallicity were reported for the NGC 7469 SB ring and outer region by Cazzoli et al. (2020) and Zamora & Díaz (2023) using optical nebular lines. However, metallicity determination is challenging at all spatial scales, particularly in AGN-affected nuclear regions where it remains unknown. Considering a CO-to-H$_2$ conversion factor accounting for both solar-like metallicity and gas excitation, as prescribed by Narayanan et al. (2012), we found that the change in slope between the SB ring and outer disk remains appreciable. A significantly decreasing metallicity gradient toward the nucleus could still mitigate the slope change in the SB$_{PAH}$–Σ_{H2} relation. However, there is no evidence for such a trend. Additionally, several factors, including grain size distribution, temperature, ionization field, metallicity, and dust amount can affect PAH luminosity (e.g., Chastenet et al. 2023; Whitcomb et al. 2024). The 7.7 μm complex is associated with larger, positively charged ions (Galliano et al. 2008;

Draine et al. 2021; Rigopoulou et al. 2021; Maragkoudakis et al. 2022), and its emission can increase around young stars due to a stronger radiation field. However, investigating PAH properties such as grain size distribution and ionization fraction involves examining the ratios between various MIR PAH features (Bohn et al. 2023; Lai et al. 2023). Finally, spatially resolved studies of nearby galaxies have reported a steepening of the radio spectral index with increasing distance from the center (e.g., Paladino et al. 2009; Basu et al. 2015; Roy & Manna 2021), with additional local variations in regions of active SF (Westcott et al. 2018). We therefore cannot exclude that the superposition of these effects could cause the observed slope change in the $\log SB_{PAH}$–$\log \Sigma_{SFR}$ relation.

4.3. The Star Formation Law

Figure 4 shows the spatially resolved SF law on a ~300 pc scale for NGC 7469. The plot also includes NGC 2992 measurements obtained with a similar method on ~200 pc scales (Zanchettin et al. 2023), and the relations derived for compilation of local AGN (Casasola et al. 2015), and ultraluminous/luminous infrared galaxies (U/LIRGs; $L_{IR} > 10^{12}$ $L_\odot$ and $>10^{11}$ $L_\odot$, respectively; Kennicutt & De Los Reyes 2021). The purple shaded area shows the K-S relation for local AGN hosts drawn from the NUclei of GAlaxies (NUGA) survey, characterized by SFR within $-0.9 < \log SFR/M_\odot yr^{-1} < 0.8$ and cold molecular gas masses in the range $8.5 < \log M(H_2)/M_\odot$ yr^{-1} < 9.6 (see Casasola et al. 2015, and references therein). The yellow shaded area shows the SF law found for dusty SBs U/LIRGs, with $1.1 < \log SFR/M_\odot yr^{-1} < 1.8$, and cold molecular gas masses $9.4 < \log M(H_2)/M_\odot$ yr^{-1} < 10.2 (Kennicutt & De Los Reyes 2021). We adopted the same fitting method as described above, taking into account the uncertainties both on Σ_{SFR} and on Σ_{H2}, and the best-fit linear relation for all data points is $\log \Sigma_{SFR} = (1.02 \pm 0.07)\log \Sigma_{H2} + (-2.85 \pm 0.02)$ (green solid line in Figure 4). The slope of this relation is consistent with that obtained

by fitting the SB ring alone, while we find a flatter slope for the fit of the outer region ($n = 0.5 \pm 0.1$). As the latter fit is dominated by data points with a low S/N, we consider the global $\log \Sigma_{SFR} - \log \Sigma_{H2}$ relation as the best fit for NGC 7469.

The SF relation derived for the NUGA AGNs (purple shaded area) exhibits a slightly steeper slope ($n = 1.14 \pm 0.01$) and a $\sim$0.6 dex offset toward lower SFR surface densities with respect to NGC 7469. Kennicutt & De Los Reyes (2021) found that SB galaxies and U/LIRGs are fitted by a linear relation with slope $n = (0.98 \pm 0.07)$, consistent with the one derived for NGC 7469 in this work, and an $\sim$0.6 dex offset in the zero-point toward higher SFR surface densities (yellow shaded area). Considering the associated errors, the slopes of the relations reported by Kennicutt & De Los Reyes (2021) and Casasola et al. (2015) are roughly consistent within 3σ. Figure 4 indicates that the individual regions of NGC 7469 occupy an intermediate area of the $\log \Sigma_{SFR} - \log \Sigma_{H2}$ plane, corresponding to an intermediate SF regime between local AGNs and U/LIRGs. The observed scatter in the data points can reflect local variations in the physical conditions of the ISM from which the stars form, such as the morphology and concentration of the gas, and any differences in gas excitation. Additionally, local fluctuations in physical quantities affect the conversion (e.g., CO-to-H_2 conversion factor and radio steepness) from observables to physical quantities. In Figure 4, we report the characteristic gas depletion timescales: the NGC 7469 data points show an average $\tau_{dep,mean} = (0.66 \pm 0.02)$ Gyr, where the uncertainty is the standard error of the mean. The measurements of the circumnuclear region of NGC 2992 (black triangles; Zanchettin et al. 2023), derived with a spatial resolution of 200 pc, populate regions of the SF law chart characterized by both relatively lower $\log \Sigma_{SFR}$ and $\log \Sigma_{H2}$, with respect to NGC 7469. The difference observed between NGC 2992 and our target may reflect the fact that individual galaxies may show different SF laws, as highlighted by Casasola et al. (2022) in their work on a set of nearby spiral DustPedia[11] galaxies. However, NGC 2992 has an average $\tau_{dep,mean} = (0.38 \pm 0.07)$ Gyr, consistent with that measured in our target.

ORCID iDs

Maria Vittoria Zanchettin https://orcid.org/0000-0001-7883-496X
Marcella Massardi https://orcid.org/0000-0002-0375-8330
Francesco Salvestrini https://orcid.org/0000-0003-4751-7421
Manuela Bischetti https://orcid.org/0000-0002-4314-021X
Chiara Feruglio https://orcid.org/0000-0002-4227-6035
Fabrizio Fiore https://orcid.org/0000-0002-4031-4157
Andrea Lapi https://orcid.org/0000-0002-4882-1735

References

Accurso, G., Saintonge, A., Catinella, B., et al. 2017, MNRAS, 470, 4750
Alberdi, A., Colina, L., Torrelles, J. M., et al. 2006, ApJ, 638, 938
Alonso-Herrero, A., Pereira-Santaella, M., Rigopoulou, D., et al. 2020, A&A, 639, A43
Arango-Toro, R. C., Ciesla, L., Ilbert, O., et al. 2023, A&A, 675, A126
Armus, L., Charmandaris, V., Bernard-Salas, J., et al. 2007, ApJ, 656, 148
Armus, L., Lai, T., U., V., et al. 2023, ApJL, 942, L37
Astropy Collaboration, Price-Whelan, A. M., Sipőcz, B. M., et al. 2018, AJ, 156, 123
Astropy Collaboration, Robitaille, T. P., Tollerud, E. J., et al. 2013, A&A, 558, A33
Basu, A., Beck, R., Schmidt, P., & Roy, S. 2015, MNRAS, 449, 3879
Belfiore, F., Leroy, A. K., Williams, T. G., et al. 2023, A&A, 678, A129
Bigiel, F., Leroy, A. K., Walter, F., et al. 2011, ApJL, 730, L13
Bohn, T., Inami, H., Diaz-Santos, T., et al. 2023, ApJL, 942, L36
Bolatto, A. D., Wolfire, M., & Leroy, A. K. 2013, ARA&A, 51, 207
Bouchet, P., García-Marín, M., Lagage, P. O., et al. 2015, PASP, 127, 612
Casasola, V., Bianchi, S., Magrini, L., et al. 2022, A&A, 668, A130
Casasola, V., Hunt, L., Combes, F., & García-Burillo, S. 2015, A&A, 577, A135
Cazzoli, S., Gil de Paz, A., Márquez, I., et al. 2020, MNRAS, 493, 3656
Chastenet, J., Sutter, J., Sandstrom, K., et al. 2023, ApJL, 944, L12
Condon, J. J., Huang, Z. P., Yin, Q. F., & Thuan, T. X. 1991, ApJ, 378, 65
Cortzen, I., Garrett, J., Magdis, G., et al. 2019, MNRAS, 482, 1618
Davies, R. I., Tacconi, L. J., & Genzel, R. 2004, ApJ, 602, 148
Dey, B., Rosolowsky, E., Cao, Y., et al. 2019, MNRAS, 488, 1926
Díaz-Santos, T., Alonso-Herrero, A., Colina, L., Ryder, S. D., & Knapen, J. H. 2007, ApJ, 661, 149
Díaz-Santos, T., Charmandaris, V., Armus, L., et al. 2010, ApJ, 723, 993
Díaz-Santos, T., Charmandaris, V., Armus, L., et al. 2011, ApJ, 741, 32
Draine, B. T., Li, A., Hensley, B. S., et al. 2021, ApJ, 917, 3
Farrah, D., Lonsdale, C. J., Weedman, D. W., et al. 2008, ApJ, 677, 957
Fathi, K., Izumi, T., Romeo, A. B., et al. 2015, ApJL, 806, L34
Ford, G. P., Gear, W. K., Smith, M. W. L., et al. 2013, ApJ, 769, 55
Foreman-Mackey, D., Hogg, D. W., Lang, D., & Goodman, J. 2013, PASP, 125, 306
Galliano, F., Madden, S. C., Tielens, A. G. G. M., Peeters, E., & Jones, A. P. 2008, ApJ, 679, 310
Genzel, R., Lutz, D., Sturm, E., et al. 1998, ApJ, 498, 579
Genzel, R., Tacconi, L. J., Gracia-Carpio, J., et al. 2010, MNRAS, 407, 2091
Genzel, R., Weitzel, L., Tacconi-Garman, L. E., et al. 1995, ApJ, 444, 129
Gioia, I. M., Gregorini, L., & Klein, U. 1982, A&A, 116, 164
Gruppioni, C., Berta, S., Spinoglio, L., et al. 2016, MNRAS, 458, 4297
Hao, C.-N., Kennicutt, R. C., Johnson, B. D., et al. 2011, ApJ, 741, 124

Izumi, T., Kohno, K., Aalto, S., et al. 2015, ApJ, 811, 39
Izumi, T., Nguyen, D. D., Imanishi, M., et al. 2020, ApJ, 898, 75
Jensen, J. J., Hönig, S. F., Rakshit, S., et al. 2017, MNRAS, 470, 3071
Kennicutt, R. C., & Evans, N. J. 2012, ARA&A, 50, 531
Kennicutt, R. C., Jr. 1998a, ApJ, 498, 541
Kennicutt, R. C., Jr. 1998b, ARA&A, 36, 189
Kennicutt, R. C., Jr., & De Los Reyes, M. A. C. 2021, ApJ, 908, 61
Klein, U., & Emerson, D. T. 1981, A&A, 94, 29
Kreckel, K., Faesi, C., Kruijssen, J. M. D., et al. 2018, ApJL, 863, L21
Lai, T. S. Y., Armus, L., Bianchin, M., et al. 2023, ApJL, 957, L26
Lai, T. S. Y., Armus, L., U., V., et al. 2022, ApJL, 941, L36
Landt, H., Bentz, M. C., Ward, M. J., et al. 2008, ApJS, 174, 282
Leroy, A. K., Bolatto, A., Gordon, K., et al. 2011, ApJ, 737, 12
Leroy, A. K., Walter, F., Sandstrom, K., et al. 2013, AJ, 146, 19
Linden, S. T., Murphy, E. J., Dong, D., et al. 2020, ApJS, 248, 25
Linden, S. T., Song, Y., Evans, A. S., et al. 2019, ApJ, 881, 70
Lonsdale, C. J., Lonsdale, C. J., Smith, H. E., & Diamond, P. J. 2003, ApJ, 592, 804
Mahajan, S., Ashby, M. L. N., Willner, S. P., et al. 2019, MNRAS, 482, 560
Maragkoudakis, A., Boersma, C., Temi, P., Bregman, J. D., & Allamandola, L. J. 2022, ApJ, 931, 38
McMullin, J. P., Waters, B., Schiebel, D., Young, W., & Golap, K. 2007, in ASP Conf. Ser. 376, Astronomical Data Analysis Software and Systems XVI, ed. R. A. Shaw, F. Hill, & D. J. Bell (San Francisco, CA: ASP), 127
Murphy, E. J., Bremseth, J., Mason, B. S., et al. 2012, ApJ, 761, 97
Murphy, E. J., Condon, J. J., Schinnerer, E., et al. 2011, ApJ, 737, 67
Narayanan, D., Krumholz, M. R., Ostriker, E. C., & Hernquist, L. 2012, MNRAS, 421, 3127
Nguyen, D. D., Izumi, T., Thater, S., et al. 2021, MNRAS, 504, 4123
Onodera, S., Kuno, N., Tosaki, T., et al. 2010, ApJL, 722, L127
Orienti, M., & Prieto, M. A. 2010, MNRAS, 401, 2599
Paladino, R., Murgia, M., & Orrù, E. 2009, A&A, 503, 747
Papadopoulos, P. P., van der Werf, P. P., Xilouris, E. M., et al. 2012, MNRAS, 426, 2601
Peeters, E., Spoon, H. W. W., & Tielens, A. G. G. M. 2004, ApJ, 613, 986
Pérez-Torres, M. A., Alberdi, A., Colina, L., et al. 2009, MNRAS, 399, 1641

Perrin, M. D., Sivaramakrishnan, A., Lajoie, C.-P., et al. 2014, Proc. SPIE, 9143, 91433X
Pessa, I., Schinnerer, E., Leroy, A. K., et al. 2022, A&A, 663, A61
Puget, J. L., & Leger, A. 1989, ARA&A, 27, 161
Riechers, D. A., Pope, A., Daddi, E., et al. 2014, ApJ, 786, 31
Rieke, G. H., Wright, G. S., Böker, T., et al. 2015, PASP, 127, 584
Rigopoulou, D., Barale, M., Clary, D. C., et al. 2021, MNRAS, 504, 5287
Roy, S., & Manna, S. 2021, MNRAS, 507, 4734
Sandstrom, K. M., Leroy, A. K., Walter, F., et al. 2013, ApJ, 777, 5
Schmidt, M. 1959, ApJ, 129, 243
Schmidt, M. 1963, ApJ, 137, 758
Schruba, A., Leroy, A. K., Walter, F., et al. 2011, AJ, 142, 37
Shao, L., Koribalski, B. S., Wang, J., Ho, L. C., & Staveley-Smith, L. 2018, MNRAS, 479, 3509
Shipley, H. V., Papovich, C., Rieke, G. H., Brown, M. J. I., & Moustakas, J. 2016, ApJ, 818, 60
Soifer, B. T., Bock, J. J., Marsh, K., et al. 2003, AJ, 126, 143
Solomon, P. M., & Vanden Bout, P. A. 2005, ARA&A, 43, 677
Song, Y., Linden, S. T., Evans, A. S., et al. 2021, ApJ, 916, 73
Sun, J., Leroy, A. K., Ostriker, E. C., et al. 2023, ApJL, 945, L19
Tabatabaei, F. S., Schinnerer, E., Krause, M., et al. 2017, ApJ, 836, 185
Teng, Y.-H., Chiang, I.-D., Sandstrom, K. M., et al. 2024, ApJ, 961, 42
Valiante, E., Lutz, D., Sturm, E., et al. 2007, ApJ, 660, 1060
Veilleux, S., Rupke, D. S. N., Kim, D. C., et al. 2009, ApJS, 182, 628
Westcott, J., Brinks, E., Hindson, L., Beswick, R., & Heesen, V. 2018, MNRAS, 475, 5116
Whitcomb, C. M., Sandstrom, K., Leroy, A., & Smith, J. D. T. 2023, ApJ, 948, 88
Whitcomb, C. M., Smith, J. D. T., Sandstrom, K., et al. 2024, arXiv:2405.09685
Williams, T. G., Lee, J. C., Larson, K. L., et al. 2024, arXiv:2401.15142
Xie, Y., & Ho, L. C. 2019, ApJ, 884, 136
Xu, X., & Wang, J. 2022, ApJ, 933, 110
Zamora, S., & Díaz, Á. 2023, arXiv:2310.12895
Zanchettin, M. V., Feruglio, C., Massardi, M., et al. 2023, A&A, 679, A88
Zhang, L., & Ho, L. C. 2023, ApJL, 953, L9